


# Theoretical Investigation and Electrochemical Study of Stoichiometric Hydroxyapatite as an Ecofriendly Corrosion Inhibitor for Steel in 3% NaCl

Nouhaila Ferraa<sup>1</sup>, Moussa Ouakki<sup>1,2,\*</sup> , Mohammed Barbouchi<sup>3</sup>, Mohammed Cherkaoui<sup>1,2</sup>, Mounia Bennani Ziatni<sup>1</sup>

<sup>1</sup> Materials, Electrochemistry and Environment team; Organic Chemistry, Catalysis and Environment Laboratory, Faculty of Science, Ibn Tofail University, PB. 133-14050 Kenitra, Morocco

<sup>2</sup> National Higher School of Chemistry (NHSC), University Ibn Tofail PO Box 133-14000, Kenitra, Morocco

<sup>3</sup> Laboratory of Molecular Chemistry and Natural Substances, Faculty of Science, Department of Chemistry, Moulay Ismail University, B.P 11201 Zitoune, Meknes, Morocco

\* Correspondence: [moussa.ouakki@uit.ac.ma](mailto:moussa.ouakki@uit.ac.ma) (M.O.);

Scopus Author ID: 57193324519

Received: 14.04.2023; Accepted: 11.08.2023; Published: 4.02.2024

**Abstract:** Saline environments are often found in cooling and water injection systems. When steel is exposed to similar environments, it gets pitting corrosion. To prevent this phenomenon, it is important to use corrosion inhibitors. This work assesses the efficacy of hydroxyapatite as a potential corrosion inhibitor for steel. This is the first application of this compound as an inhibitor in a saline environment. The synthesized product was investigated using X-ray diffraction, Fourier Transform Infrared Spectroscopy, chemical analysis, and SEM/EDX to characterize its properties and morphology. The inhibitory efficiency of HAp in NaCl, 3% medium, was performed by electrochemical techniques, including the stationary polarisation curves (PDP), open circuit potential (OCP), and electrochemical impedance spectroscopy (EIS). The synthesized product is hydroxyapatite with a Ca/P ratio of 1.67. The electrochemical study revealed that HAp is capable of preventing corrosion in 3% NaCl, with an inhibitory efficiency exceeding 91% when the inhibitor concentration is at 100 ppm. Also, the type of inhibitor is predominantly mixed with cathodic. The HAp molecule's adsorption is in accordance with the Langmuir adsorption isotherm. Also, the SEM/EDX analysis of the metal surface indicates that a barrier film is formed at the interface steel/NaCl, which is made up of the primary elements of HAp. The theoretical aspect was carried out through density functional theory (DFT) and molecular dynamics (MD) simulation. The outcomes of the theoretical approach (DFT and MD simulations) confirm all the experimental results by showing the analogous tendency of the synthesized material's inhibition efficiency and indicating that HAp can act as an excellent steel inhibitor in 3% NaCl.

**Keywords:** corrosion; inhibitor; Hap; theoretical approach

© 2024 by the authors. This article is an open-access article distributed under the terms and conditions of the Creative Commons Attribution (CC BY) license (<https://creativecommons.org/licenses/by/4.0/>).

## 1. Introduction

Hydroxyapatite is a biomaterial that finds extensive use in diverse medical fields, including orthopedics, implantology, and others [1–3]. It has a crucial role in several fields because of its biocompatibility and biological and chemical affinity towards bone tissue.

Its ability to adsorb and exchange ions of the same or different charge in the biological medium increases its anticorrosive performance in vivo by releasing inhibitory substances that protect metal implants against corrosion and that the human body needs [4,5].

Their anticorrosive property and their non-toxic chemical formula have led researchers to evaluate them against metallic corrosion found in most industries, which causes serious damage every year due to aggressive environments [6–8]. Steel is one of the metallic materials affected by the corrosion phenomenon [9–12].

The synthesis of hydroxyapatite with a formula close to those of biological apatites was carried out by simple precipitation at room temperature in an aqueous medium [13,14]. It is necessary to mention that the Ca/P ratio of hydroxyapatite varies between 1.5 and 1.67 for non-stoichiometric ones. For the stoichiometric hydroxyapatite of formula  $\text{Ca}_{10}(\text{PO}_4)_6(\text{OH})_2$ , its ratio is equal to 1.67.

In my current research, we were interested in the synthesis and characterization of hydroxyapatite. It was investigated as a steel corrosion inhibitor in a 3% NaCl medium. According to the literature, hydroxyapatite was used for the first time as an environmentally friendly steel inhibitor in a saline environment.

The realization of this work involved different techniques of characterization of the studied inhibitor, such as XRD, FTIR, SEM/EDX, and chemical analysis to identify the atomic ratio Ca/P corresponds to the hydroxyapatite.

The performance of HAp against steel corrosion in 3% NaCl was figured out through electrochemical techniques such as electrochemical impedance spectroscopy (EIS), open circuit potential (OCP), and stationary polarization curves (PDP). This study was completed by surface analysis using SEM/EDX. In addition, the electrochemical behavior and the type of adsorption of HAp in 3% NaCl were studied using the Langmuir adsorption model, as well as the calculation of different thermodynamic parameters of the electrochemical system studied. To confirm the electrochemical results, theoretical studies have also been performed.

## 2. Materials and Methods

### 2.1. *The synthesis of the inhibitor.*

The hydroxyapatite was obtained through a co-precipitation method described by Rey et al. in 1989 [13]. This method involves using a combination of solutions A and B, where solution A is composed of 6.5 g of ammonium hydrogen phosphate, 325 ml of distilled water, and 375 ml of ammoniac, which is then rapidly added to solution B consisting of 11.75 g of calcium nitrate and 137.5 ml of distilled water at room temperature. The precipitate is separated by Büchner filtration and then washed quickly with a washing solution (3L of distilled water with 15 ml of ammoniac) before being dried at 80°C for approximately 24 hours.

### 2.2. *Characterization methods.*

#### 2.2.1. FTIR spectroscopy.

The different HAp bands were identified using FTIR analysis in the Wavelength area of  $4000\text{--}400\text{ cm}^{-1}$  using a BRUKER-type spectrometer by scattering the HAp powder on an ATR-A225 diamond at room temperature.

#### 2.2.2. X-Ray diffraction.

The X-ray diffraction spectra were obtained using a Panalytical X Pert 3 Powder diffractometer in the range 20–80 of  $2\theta$  with a step size of 0.05 and an acquisition time of 3 seconds per step, using copper  $\text{K}_\alpha$  radiation ( $\text{K}_{\alpha 1} = 1.5405980\text{ \AA}$ ).

### 2.2.3. MEB/EDX.

The morphology surface of the synthesized phosphate and the steel substrate after exposure to NaCl medium with and without HAp was investigated using Quantro S-Feg-Thermofisher Scientific scanning electron microscope related to X-ray energy dispersive analysis.

### 2.2.4. Chemical analysis.

To determine the Ca/P atomic ratio that characterizes the prepared HAp powder, the quantification of phosphorus ions was carried out by colorimetry [14] using a ZUZI Model 4201/50 UV-visible spectrophotometer and of calcium ions by titration in the presence of EDTA in a basic medium.

## 2.3. Material preparation.

Steel is used for the electrochemical tests with a specific exposed surface area of 1 cm<sup>2</sup>. It is formed by the following elements (wt%): Mn: 0.47%, Si: 0.24%, C: 0.11%, Cu: 0.14%, Al: 0.03%, Mo: 0.02%, Cr: 0.01%, Ni: 0.1%, W: 0.06%, V: <0.003%, Co: <0.0012%, and the remaining element is Fe. Before each electrochemical test, the steel substrates were treated using abrasive paper with different granulations. Then wash with acetone to remove the grease and with distilled water. The aggressive medium is NaCl 3%, prepared by dissolving 30 g of NaCl powder in 1L of distilled water.

## 2.4. Electrochemical study.

A three-electrode cell attached to a potentiostat/galvanostat PGZ100 was used for the electrochemical analysis. The steel plate was used as a working electrode with an exposed surface area of 1 cm<sup>2</sup>. The reference electrode was Ag/AgCl, and the counter electrode was a platinum grid.

The anodic and cathodic polarization plots were studied at a scan rate of 1 mV/s after the potential had stabilized for 30 min. The potential range was from -1200 mV to 300 mV.

The EIS patterns were obtained in the frequency range of 100 kHz to 10 mHz with an amplitude of 10 mV.ms. Before the EIS spectra were recorded, the metal was immersed for 30 min.

## 2.5. Theoretical investigations.

### 2.5.1. Quantum chemical calculations.

We performed DFT calculations to elucidate hydroxyapatite's adsorption behavior on the steel substrate. DFT was achieved by the Gaussian 09 package program using the B3LYP functional [15]. In addition, the GaussView 5.0.8 program was employed to generate molecular structure and visualization of results. The optimization calculation of hydroxyapatite was carried out using 6-311++G(d, p) basis. The impact of water was simulated with the self-consistent reaction field (SCRf) calculations by using the polarizable continuum model (PCM) [16]. Several theoretical indices are included in the analysis of the electronic properties of inhibitors: energy band gap ( $\Delta E_{gap}$ ), frontier molecular orbitals ( $E_{LUMO}$  and  $E_{HOMO}$ ), electronegativity ( $\chi$ ), fraction of electron transfer ( $\Delta N$ ), ionization potential ( $I_P$ ), electron

affinity ( $E_A$ ), hardness ( $\eta$ ), global electrophilicity ( $\omega$ ), softness ( $\sigma$ ) and nucleophilicity ( $\varepsilon$ ). Using the following relations given below [17,18], the computational parameters can be determined from the values of  $E_{LUMO}$  and  $E_{HOMO}$ .

Calculations of the Fukui Indices (FI) were performed with the Material Studio version 7.0 program from Accelrys Inc. The DMol3 module was embedded into this software and used for performing GGA (generalized gradient approximation) of Perdew-Burke Ernzerhof (PBE) and "double numerical plus numerical polarization (DNP) settings 4.4. This calculation was performed by Chugh et al [19]. Dmol3's default convergence criteria define the quality of DFT calculations as "fine." Fukui functions were calculated through Hirshfeld population analysis.

$$\Delta E_{gap} = E_{LUMO} - E_{HOMO} \tag{1}$$

$$\Delta N_{110} = \frac{\phi - \chi_{inh}}{2(\eta_{Fe} + \eta_{inh})} \tag{2}$$

The function  $\phi$  is the electronegativity of the metal surface, the Fe (110) surface it gives 4.82 eV.

$$\chi = \frac{I_p + E_A}{2} \tag{3}$$

$$\eta = \frac{I_p - E_A}{2} \tag{4}$$

Where the  $I_p = -E_{HOMO}$  and  $E_A = -E_{LUMO}$ .

$$\omega = \frac{\mu^2}{2\eta} \tag{5}$$

Where  $\mu = ((E_{LUMO} + E_{HOMO})/2)$  is the electronic chemical potential

$$\varepsilon = \frac{1}{\omega} \tag{6}$$

$$\sigma = \frac{1}{\eta} \tag{7}$$

### 2.5.2. Molecular dynamics simulations.

The intermolecular interaction of hydroxyapatite inhibiting with steel substrate and their adsorption behavior was analyzed by molecular simulations. The MD approach implemented in Materials Studio software (Studio, n.d.) was adopted. Using Fe (110) supercell of size (12 × 12), a vacuum space 5 nm, the iron substrate was taken into consideration, and a vacuum slab of 30 Å thickness was built above the iron (110). The iron (110) surface was selected due to its most stable geometry [20]. In addition, for performing the MD simulations, first, a solution medium was built through water cell construction at its experimental density, which contains 500 H<sub>2</sub>O, 5 ions (Na<sup>+</sup> and Cl<sup>-</sup>), and one inhibitor molecule reflecting the experimentally used neutral chloride media[21]. The simulation was done using COMPASS force field [22] for 500000 steps using a smart minimizer in the Materials Studio pack's Forcite module. This was followed by 500 ps NVT MD simulations executed with 1 fs time. In addition, a radius of 12.5 Å, along with an atom-based cutoff, was applied for the van der Waals interaction calculations. In NVT simulations, the Nose-Hoover thermostat was used to keep the temperature at 298 K. We used equations 8 and 9 to estimate the interaction strength through the interaction energy and the total binding energy, respectively [23].

$$E_{interaction} = E_{total} - (E_{surface+solution} + E_{inhibitor}) \tag{8}$$

$$E_{binding} = -E_{interaction} \tag{9}$$

Where  $E_{surface+solution}$  is the total energy of Fe (1 1 0) surface and solution without the inhibitor and  $E_{inhibitor}$  denote the total energy of inhibitor;  $E_{total}$  shows the total energy of the whole system.

### 3. Results and Discussion

#### 3.1. Characterization of hydroxyapatite.

##### 3.1.1. FTIR.

The infrared spectrum obtained is represented in Fig. 1. All the characteristic bands of the phosphate prepared are observed. A wide stretching vibration of the hydroxyle group ( $\text{OH}^-$ ) was detected around  $3529 \text{ cm}^{-1}$ . Also, the presence of characteristic bands of  $\text{PO}_4$  groups is located between  $1004\text{-}473 \text{ cm}^{-1}$ . In particular, the band at around  $1004 \text{ cm}^{-1}$  corresponds to P-O's symmetrical and antisymmetrical stretching vibration. The bands near  $568.3 \text{ cm}^{-1}$  and  $472.9 \text{ cm}^{-1}$  are related to the bending vibration of O-P-O [7,24].

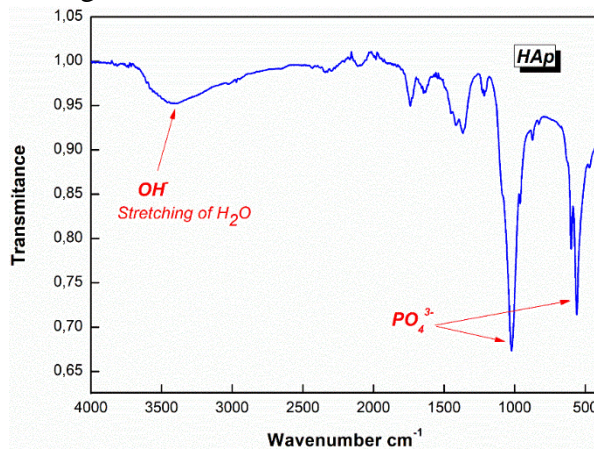


**Figure 1.** FT-IR spectrum of synthesized Hap.

##### 3.1.2. X-ray diffraction.

The X-ray diffraction of the synthesized material was studied. The Fig. 2 shows the diffractogram of  $\text{Ca}_{10}(\text{PO}_4)_6(\text{OH})_2$ . The different peaks of the hydroxyapatite are identified (JCPDS card 901-0051).

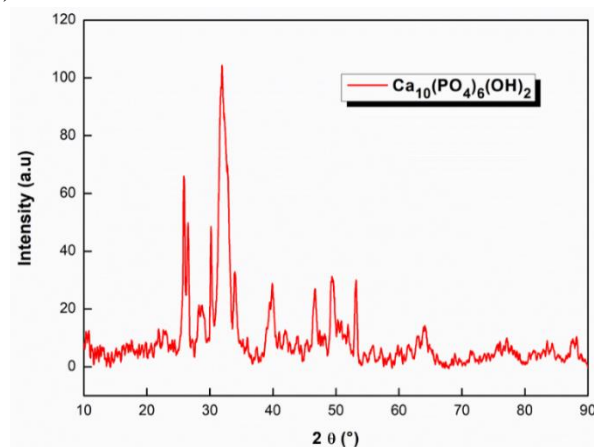


**Figure 2.** X-ray diffraction spectrum of  $\text{Ca}_{10}(\text{PO}_4)_6(\text{OH})_2$ .



### 3.1.3. SEM/EDX.

The morphology of HAp powder was performed through scanning electron microscopy (SEM) related to X-ray energy dispersive analysis (EDX). The results are shown in Fig. 3. A dispersion of varying-sized particles is observed throughout the surface with the same view characterizing an apatite. The observation of phosphate and calcium peaks in the EDX spectra indicates that the product is a calcium phosphate, and the intensity ratio is specific to the hydroxyapatite prepared.

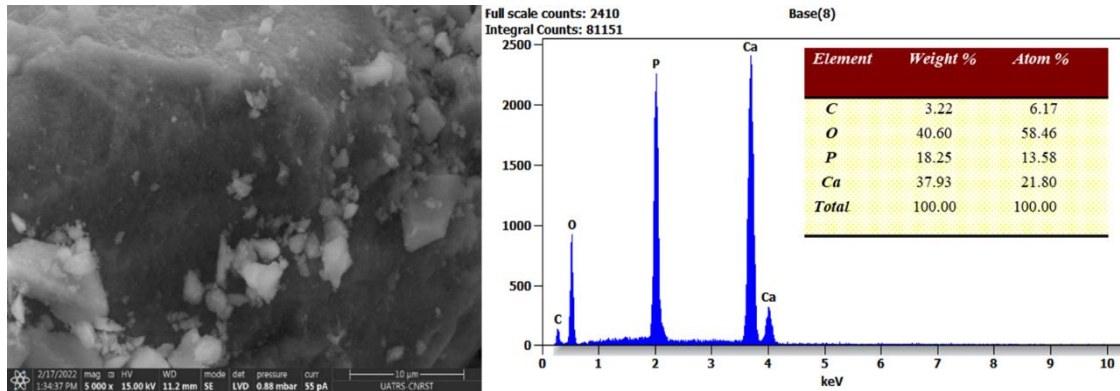


**Figure 3.** Morphology and EDX spectrum of HAp powder.

### 3.1.4. Chemical analysis.

To verify the Ca/P atomic ratio of the HAp, we performed a quantitative analysis of phosphorus and calcium ions in solution. The concentrations of these ions were measured three times with a precision of approximately 0.05. As shown in Table 1, the experimental results revealed a Ca/P ratio equal to 1.67, consistent with the Ca/P ratio of hydroxyapatite[24].

**Table 1.** Concentration of calcium, phosphorus, and Ca/P ratio of HAp.

Compound	[Ca <sup>2+</sup> ] (mmol/L)	[PO <sub>4</sub> <sup>3-</sup> ] (mmol/L)	Rapport Ca/P
HAp	8,6±0.05	5,13±0.05	1,67±0.01

## 3.2. Electrochemical study.

### 3.2.1. Open circuit potential (OCP).

The variation of E<sub>ocp</sub> of the steel versus the immersion time in 3% NaCl is shown in Fig. 4, with and without the HAp inhibitor. The uninhibited solution indicates a significant potential shift from the beginning of the curve, probably due to the high dissolution of the steel substrate in 3% NaCl [25].

In the existence of HAp at different concentrations, the potential values are shifted slightly. This can be attributed to a delay in the anodic process at the interface. This effect is explained by the high inhibiting effect of HAp against steel, which is observed at a concentration of 100 ppm. These findings are broadly related to the adsorption of material inhibitors to steel [26].

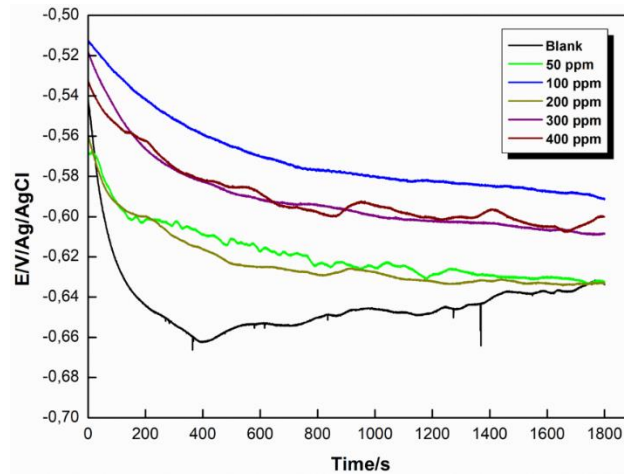


**Figure 4.** Open circuit potential of steel in 3% NaCl in the presence and absence of HAp.

3.2.2. Polarization curves.

Figure 5 presents the TAFEL plots of the metal in a 3% NaCl medium, with and without the presence of HAp at 298 K. The results indicate that HAp does not alter the shape of the anodic and cathodic curves compared with the blank solution. This indicates that the presence of HAp in the corrosive medium leads to a decrease in the steel dissolution rates and hydrogen reduction reactions.

The cathodic side has been divided into three distinct parts—the first part between  $E_{corr}$  and the potential for the plateau's start. The dominant reaction is the reduction of oxygen (reaction 10). The second part characterizes oxygen diffusion, and the third part is related to the reduction of water (reaction 11) [7,27].



For the anodic part, it is a reaction of dissolution of the iron (reaction 12):



Furthermore, we noticed that in the presence of HAp, the corrosion potential is shifted towards more cathodic values than the reference sample. The corrosion current density is reduced for an optimal value in a concentration equal to 100 ppm [28].

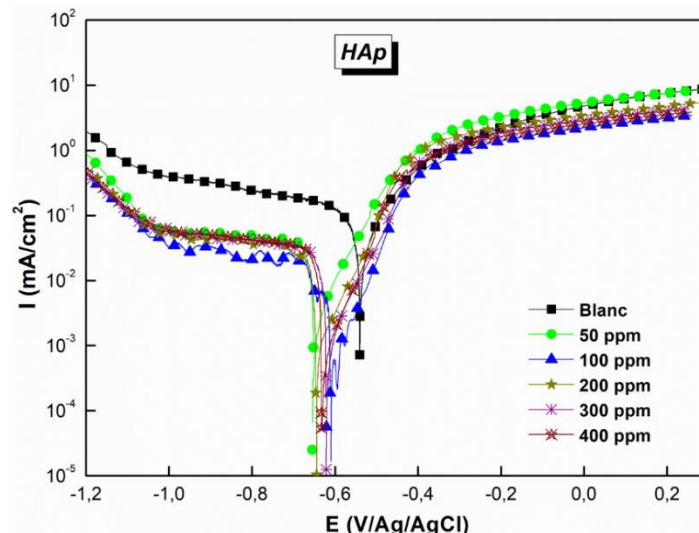


**Figure 5.** TAFEL polarization curves for HAp at the 3% steel/NaCl interface at 298 k.

From the extrapolation of the cathodic and anodic curves, we can obtain the electrochemical parameters such as the cathodic ( $\beta_c$ ) and anodic ( $\beta_a$ ) slopes, corrosion potential ( $E_{corr}$ ), and the corrosion current density ( $i_{corr}$ ). These parameters were collected in Table 3 with the inhibitory efficiency  $\eta_{pp}$ (%) for each HAp concentration calculated by the following relationship (13):

$$\eta_{pp}(\%) = \frac{I_{corr,0} - I_{corr}}{I_{corr}} \times 100 \tag{13}$$

With  $I_{corr,0}$  and  $I_{corr}$  represent the corrosion current densities with and without HAp in 3% NaCl, respectively.

**Table 3.** Electrochemical polarization parameters of the steel in NaCl 3% without and with the presence of HAp.

Medium	[Inh] ppm	- $E_{corr}$ mV/Ag/AgCl	$i_{corr}$ ( $\mu A\ cm^{-2}$ )	- $\beta_c$ (mV dec <sup>-1</sup> )	$\beta_a$ (mV dec <sup>-1</sup> )	$\eta_{pp}$ %
NaCl 3%	--	538	464	141	149	-
HAp	50	648	154.7	150	132	66.6
	100	609	40.4	139	128	91.3
	200	645	75.9	135	124	83.6
	300	620	79.5	131	127	82.8
	400	631	90.2	126	130	80.5

The parameters in Table 3 show that the  $I_{corr}$  decreased after adding HAp. It decreased from  $464\ \mu A\ cm^{-2}$  for the blank solution to  $40.4\ \mu A\ cm^{-2}$  for an optimum concentration of 100 ppm HAp [29]. The inhibitory efficiency increases significantly at this same concentration and reaches 91.3%. Beyond 100 ppm, the inhibitory efficiency has slightly decreased but is still significant. Nonetheless, the  $I_{corr}$  increases.

The corrosion potential values have slightly shifted in the presence of HAp compared to the blank. Nevertheless, this deviation was less than  $\pm 85\ mV$  [30], which indicates that our inhibitor acts as a mixed type with cathodic predominance in NaCl 3 % [31,32].

### 3.2.3 Impedance diagrams.

The behavior of steel in 3% NaCl solution was also examined by electrochemical impedance. The results were represented through NYQUIST diagrams after 30 minutes of immersion at 298 K. The impedance diagrams are shown in Figure 6.

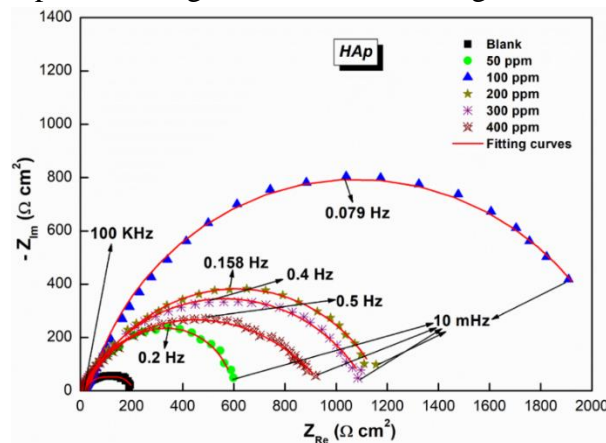


**Figure 6.** NYQUIST impedance diagram of steel in 3% NaCl medium in the absence and presence of HAp at different concentrations.



From Fig. 6, the size of the capacitive loop increases in the presence of HAp compared to the NaCl medium; it reaches a maximum of 100 ppm of the inhibitor.

The NYQUIST diagrams of steel in 3% NaCl and after the addition of HAp show two overlapping capacitive loops; the first one at high frequency indicates the formation of a protective film on the metal surface, and the second one at low frequency related to the charge transfer phenomenon [7,8]. This finding is confirmed by the BODE diagrams illustrated in Fig. 7, which show a phase widening in the presence of different HAp concentrations[33,34], showing two-time constants. They are linked to two relative relaxation processes at the steel/HAp interface due to the HAp molecule's adsorption [29].

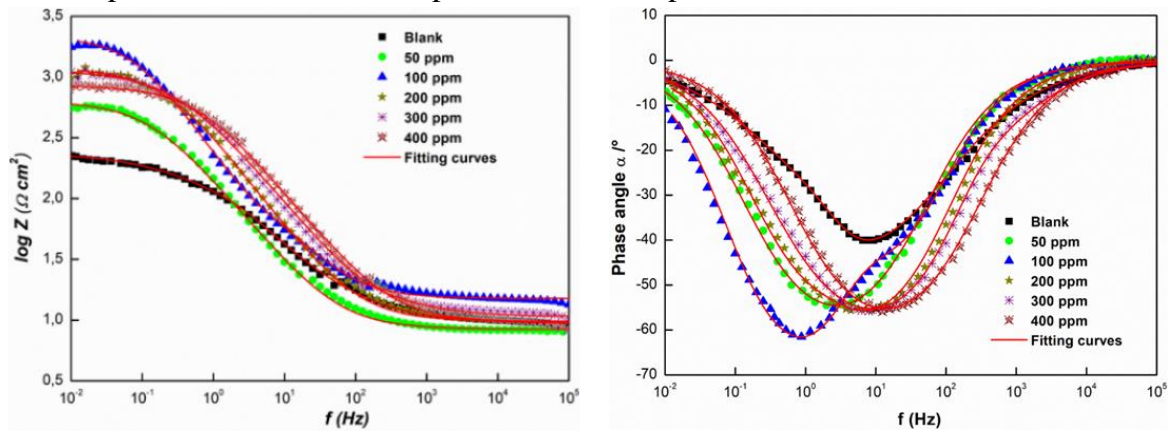


Figure 7. BODE diagrams of steel in 3% NaCl with and without HAp.

Using an appropriate equivalent circuit (Fig. 8) to fit the EIS curves makes it possible to obtain several electrochemical parameters. These include the charge transfer resistance ( $R_{ct}$ ), film resistance ( $R_f$ ), electrolyte resistance ( $R_s$ ), and constant phase elements ( $Q_f$  and  $Q_{ct}$ ), which are used instead of the film ( $C_f$ ) and double layer capacitance ( $C_{dl}$ ), respectively. They are given in Table 4.

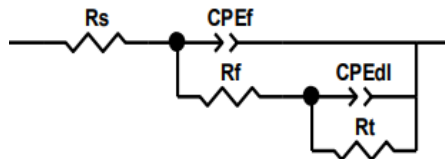


Figure 8. The equivalent circuit used for EIS curve fitting.

The expression for the CPE impedance is given by:

$$Z_{CPE}(\omega) = Q^{-1}(j\omega)^{-n} \tag{14}$$

Where Q is the proportionality coefficient of the CPE, j is the imaginary number ( $j^2=-1$ ),  $\omega$  is the angular frequency (in  $\text{rad s}^{-1}$ ), and n is the deviation parameter attributed to the phase shift, which is between 0 and 1. The electrochemical parameters are shown in Table 4.

Table 4. Electrochemical impedance parameters relative to the steel/NaCl 3% interface in the presence and absence of HAp.

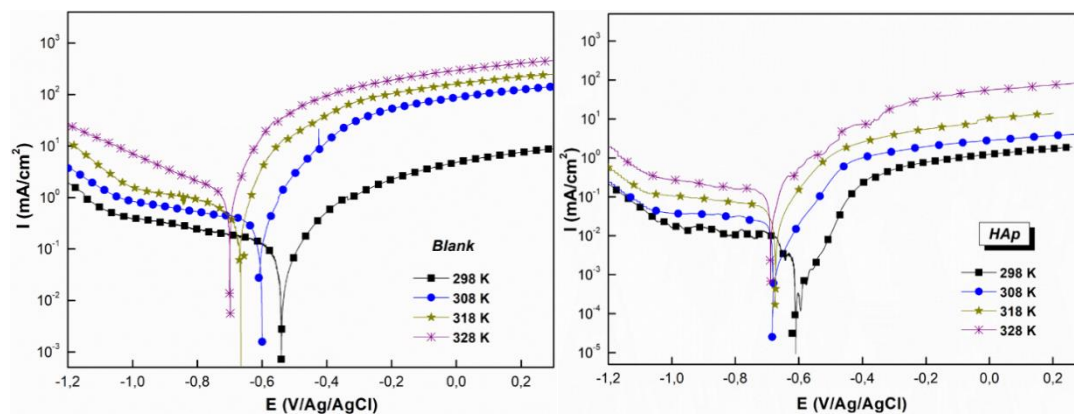
Medium	[Inh] ppm	$R_s$ ( $\Omega \text{ cm}^2$ )	$R_f$ ( $\Omega \text{ cm}^2$ )	$n_f$	$Q_f$ ( $\mu\text{F.S}^{n-1}$ )	$R_{ct}$ ( $\Omega \text{ cm}^2$ )	$n_{ct}$	$Q_{ct}$ ( $\mu\text{F.S}^{n-1}$ )	$R_p$ ( $\Omega \text{ cm}^2$ )	$\theta$	$\eta_{imp}$ %
NaCl 3%	--	10.2	161.0	0.705	1399	38.0	1	1451	199.0	-	-
HAp	50	11.9	80.8	0.958	2039	505.6	1	1239	586.4	0.660	66.0
	100	15.0	147.5	0.771	651	1993.0	0.952	288	2140.5	0.907	90.7
	200	9.7	639.8	0.757	446	536.3	1	744	1176.1	0.831	83.1
	300	10.6	219.2	0.689	546	907.4	0.952	307	1126.6	0.823	82.3
	400	7.4	110.5	0.566	448	857	0.950	80	967.5	0.794	79.4

Table 4 shows that the presence of HAp in the corrosive solution increases charge transfer resistance for all concentrations, up to a maximum value of  $1993.0 \Omega \text{ cm}^2$  at 100 ppm of the inhibitor [35]. This increase is related to a decrease in  $Q_{ct}$  values and an increase in  $R_f$  values, indicating the formation of a protective layer on the metal surface composed of HAp molecules [36]. At a concentration of 100 ppm, this film is uniform and adds better protection against corrosion. However, the inhibitory efficiency of HAp reaches its highest level of 90.7 % at this concentration.

We can also find that the values of  $n$  vary from 0.950 to 1 in the presence of the inhibitor, which led to an improvement in the surface homogeneity of the steel. This improvement is attributed to the HAp molecule adsorbing at the interface between the steel and the inhibitor [37].

### 3.2.4. Temperature effect.

To evaluate the behavior of this inhibitor at higher temperatures, polarization curves were plotted for 100 ppm HAp at different temperatures from 298K to 328K (Fig. 9). The electrochemical parameters are reported in Table 5 with the  $E_{corr}$ ,  $i_{corr}$ ,  $\beta_c$ , and  $\beta_a$  are the corrosion potential, corrosion current density and the cathodic and anodic slopes respectively.



**Figure 9.** TAFEL polarization curve of steel with and without the addition HAp at different temperatures.

Fig. 9 shows a shift in corrosion potential when the temperature increases, in the presence of 100 ppm HAp and for the blank. However, the curves' shape has not changed, which means that the temperature does not affect the mechanism [38].

**Table 5.** Electrochemical impedance parameters of the steel /surface with and without HAp.

Medium	Temperature (K)	$-E_{corr}$ (mV/Ag/AgCl)	$i_{corr}$ ( $\mu\text{A cm}^{-2}$ )	$-\beta_c$ (mV dec <sup>-1</sup> )	$\beta_a$ (mV dec <sup>-1</sup> )	$\eta_{PP}$ (%)
NaCl 3%	298	538	464	141	149	-
	308	594	758	151	154	-
	318	664	1353	160	158	-
	328	696	2170	165	161	-
HAp	298	609	40.4	139	128	91.3
	308	677	84.9	154	145	88.8
	318	668	192.6	168	152	85.7
	328	687	378.5	151	160	82.5

We also noticed that the current density of corrosion increased with temperature increase. This was confirmed by the parameters mentioned in Table 5. The  $I_{corr}$  increases from  $40 \mu\text{A cm}^{-2}$  (298 K) to  $378.5 \mu\text{A cm}^{-2}$  (328 K) in the presence of HAp[39]. In parallel, the

inhibitory efficiency slightly decreases, which means that the desorption phenomenon is more enhanced than the adsorption by changing the temperature.

3.3. Thermodynamic activation parameters.

From the ARRHENIUS equations (15) and (16), which relate the corrosion rate and the activation energy, we can calculate the different thermodynamic parameters of a corrosion reaction (Fig. 10).

$$\ln(i_{\text{corr}}) = \ln(A) - \frac{E_a}{RT} \tag{15}$$

$$\ln\left(\frac{i_{\text{corr}}}{T}\right) = \left(\ln\left(\frac{R}{Nh}\right) + \frac{\Delta S_a}{R}\right) - \frac{\Delta H_a}{RT} \tag{16}$$

Where A,  $i_{\text{corr}}$ ,  $E_a$ , R, T,  $\Delta S_a$ ,  $\Delta H_a$ , N, and h are the constant (pre-exponential factor), the corrosion current density, the activation energy, the molar constant of perfect gases, the temperature, the entropy of activation, the enthalpy of activation, the Avogadro number and the plank constant

The ARRHENIUS lines obtained with and without HAp at 100 ppm are presented in Fig. 9. The  $E_a$ ,  $\Delta S_a$ , and  $\Delta H_a$  were calculated using a linear regression of  $\ln(i_{\text{corr}})$  and  $\ln(i_{\text{corr}}/T)$  against  $1000/T$ . They have been collected in Table 5.

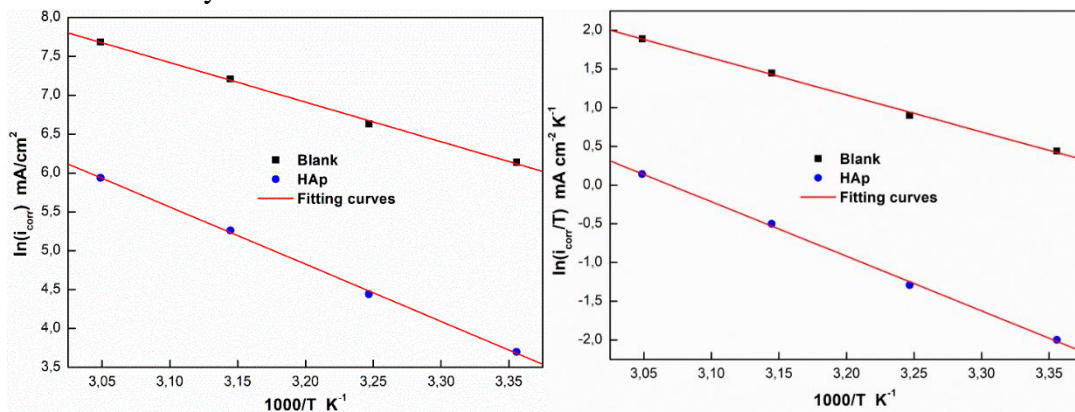


Figure 10. ARRHENIUS lines of steel with and without HAp at 100 ppm.

Table 5. Thermodynamic activation parameters of steel in 3% NaCl in the presence and absence of HAp.

Medium	[inh]	$E_a$ (KJ/mol)	$\Delta H_a$ (KJ/mol)	$\Delta S_a$ (J/mol.K)
NaCl 3%	Blank	42.3	39.7	-60.8
	HAp	61.2	58.6	-17.6

According to Fig. 10 and the data in Table 5, the  $E_a$  in the existence of HAp is greater than that in the Blank medium. This observation revealed better adsorption of HAp on the steel surface [40]. The increase in the activation energy value with the addition of the hydroxyapatite material can also be explained by the electrostatic interactions between the metal and the electrolyte medium, which form a physical barrier at the interface between the metal and the electrolyte medium [35].

Moreover, the steel surface is becoming more ordered, which can be explained by the negative values of  $\Delta S_a$ . A positive value of  $\Delta H_a$  proves that the adsorption process is endothermic [11]. Thus, it appeared that  $\Delta H_a$  was increased in the presence of HAp ed to the value found in the case of the blank medium. This means that the steel dissolution in the corrosive solution was decreased by adding HAp. All these thermodynamic results indicate that HAp blocks the corrosion reaction by forming a protective film.

The calculation of the difference between the activation energy and the activation enthalpy ( $E_a - \Delta H_a$ ) gives a value equal to  $2.6 \text{ kJ}\cdot\text{mol}^{-1}$ ; this value is near to the moderate value of  $RT$ , which is  $2.63 \text{ kJ}\cdot\text{mol}^{-1}$ . Since equation (17) is verified, we can conclude that the corrosion process is unimolecular.

$$E_a - \Delta H_a = RT \tag{17}$$

### 3.4. Langmuir adsorption.

The Langmuir model is used to investigate the behavior and the adsorption type of HAp on the metal surface [41,42]. The graphical representation giving  $C_{inh}/\theta$  versus  $C_{inh}$  is shown in Fig. 11. The inhibitor concentration is related to  $\theta$  by the following equation (18) :

$$\frac{C_{inh}}{\theta} = \frac{1}{K_{ads}} + C_{inh} \tag{18}$$

Where  $K_{ads}$  is the adsorption constant in  $\text{l/g}$ ,  $C_{inh}$  denotes the HAp concentration in  $\text{g/l}$ , and  $\theta$  represents the recovery coefficient.

From Fig. 11, we observed that the regression coefficient is near 1, which makes the Langmuir model the most appropriate to define the adsorption mode of HAp on the steel surface.

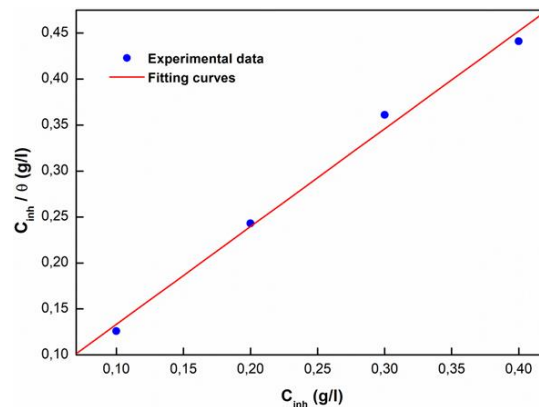


**Figure 11.** Langmuir adsorption isotherm of HAp at 298 K.

The  $K_{ads}$  were calculated from the curve  $C_{inh} / \theta$  as a function of  $C_{inh}$ ; it is linked to the standard free energy  $\Delta G_{ads}$  by the equation (19):

$$\Delta G_{ads}^{\circ} = -RT \ln(1000 \times K_{ads}) \tag{19}$$

With 1000, T and R respectively represent the water mass concentration in  $\text{g/L}$ , the temperature in K, and the perfect gas constant. The adsorption parameters are shown in the table 6.

**Table 6.** Langmuir adsorption parameters of HAp in 3% NaCl.

Compound	$K_{ads}$ (L/g)	$\Delta G_{ads}$ (Kj/mol)	$R^2$	Slope
HAp	37.12	-26.07	0.99631	1.06

According to Table 6, a higher  $K_{ads}$  value indicates the high adsorption capacity of HAp on the metal surface. As a result, their high inhibition efficiency [42].

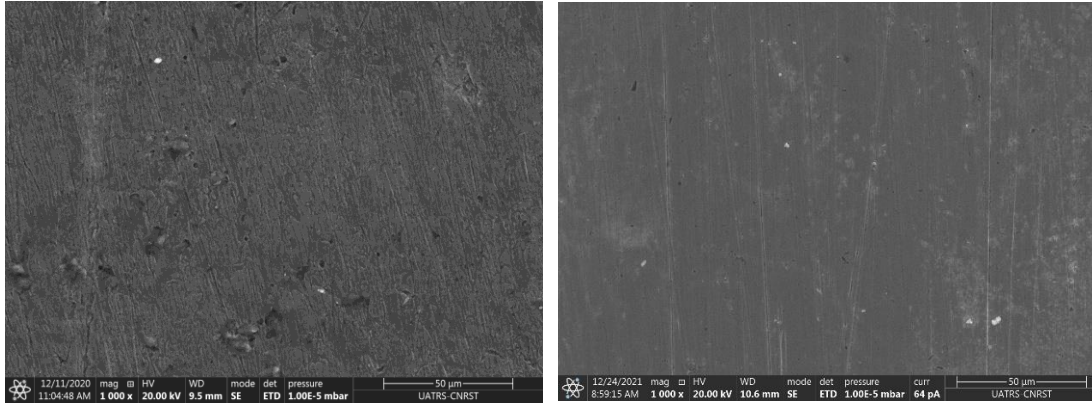
The  $\Delta G_{ads}$  negative value ( $-26.07 \text{ Kj/mol}$ ) [32] shows that the adsorption of the HAp at the interface is spontaneous.

It is known from the literature that when  $\Delta G_{ads}$  is equal to  $-40 \text{ kJ}\cdot\text{mol}^{-1}$  (more negative), it is suggested that the adsorption of the inhibitor onto the metal surface is chemical type

(coordinate bonds) [29,43]. Conversely, for values equal to  $-20 \text{ kJ}\cdot\text{mol}^{-1}$  or more, the adsorption is probably based on electrostatic interactions (physisorption). Our results conclude that the HAp adsorption on the steel is a mixed type (physical and chemical) [26,32].

### 3.5. SEM/EDX.

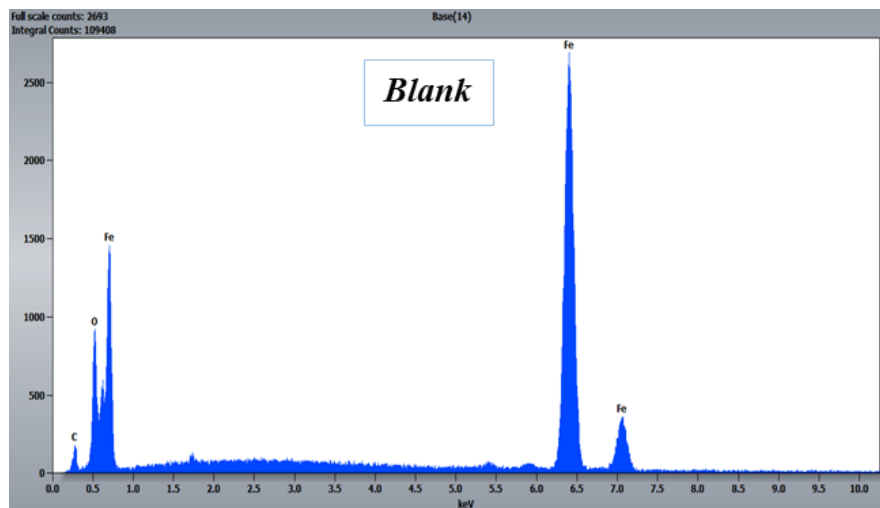
The morphology of the steel, with and without 100 ppm of HAp, after 24h of immersion in 3% NaCl was studied using SEM/EDX analysis. The morphology surface of the metal after analysis is shown in Fig. 12.



**Figure 12.** Steel morphology surface in the presence and the absence of 100 ppm HAp at room temperature.

From Fig. 12, we noticed that the surface exhibits serious damage without HAp. The appearance of cracks on the steel surface justified this. In the presence of HAp at 100 ppm, the surface was clear, and no cracks or holes were detected, corresponding to remarkable HAp protection. This observed protection could result from forming a layer made up of the HAp molecules that form on the steel surface that reduces and prevents the metal dissolution in the 3% NaCl.

The EDX spectra mentioned in Fig. 13 with and without HAp show the appearance of the elements that may exist in the steel/electrolyte medium interface. The mass percentages have been grouped in Table 7 for the 3% NaCl medium and in the presence of 100 ppm of HAp at 298 K.





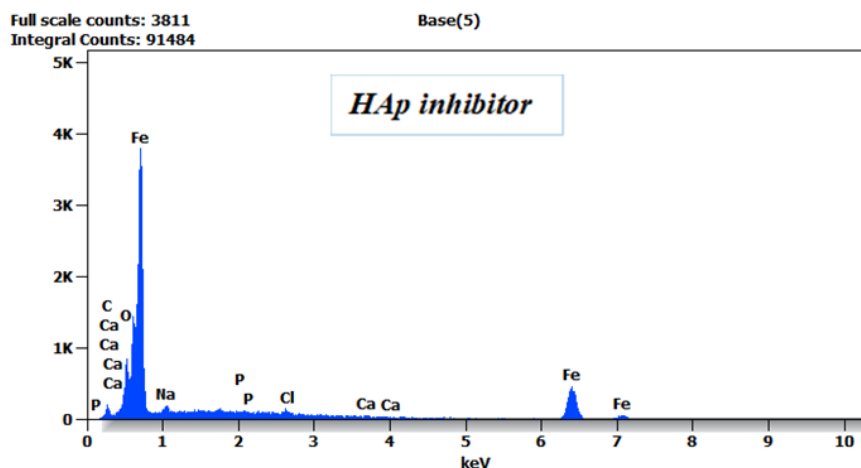


**Figure 13.** EDX analysis of the steel surface in the absence and presence of 100 ppm HAp.

The EDX spectrum of the metal in the uninhibited medium shows two intense iron peaks, which means that the surface of the metal is covered with corrosive elements like iron oxides. The presence of HAp in the corrosive medium significantly decreases the intensity of the iron peak with the appearance of calcium and phosphorus peaks over the whole surface, characteristic of the inhibitor. Also, there is a decrease in the oxygen peak when the inhibitor exists compared to the blank medium. These findings were verified by the existence of some elements (Table 7) on the metal surface.

**Table 7.** Mass percentage of some steel surface elements in the absence and presence of Hap.

Medium	Element in mass percentage %				
	Carbon	Oxygen	Calcium	Phosphor	Iron
Blank	0.98	10.07	-	-	88.95
HAp	1.16	7.52	0.14	0.25	90.93

In Table 7, we observe that the oxygen was reduced from 10.07 % to 7.52 % in the presence of HAp, with the appearance of relative percentages of calcium and phosphorus that confirm the existence of an inhibitory layer formed from the HAp molecules at the steel/medium interface, which reduces the access of corrosive substances into the steel surface.

### 3.6. Theoretical investigations.

#### 3.6.1. Quantum chemical calculations.

DFT calculations are useful for understanding corrosion inhibition effectiveness to explain inhibitor/surface interactions. It is understood that molecules with low  $E_{LUMO}$  values are more likely to accept electrons, while those with high  $E_{HOMO}$  values tend to give away electrons (Fig. 14) [44]. Moreover, it has been noted that molecules with high  $E_{HOMO}$  values tend to donate electrons to empty acceptors orbital having low energies (such as the metal Fe). From the increasing value of  $E_{HOMO}$  (Table 8), the variation order of the level of inhibition efficiency of the HAp molecule in water is greater than that in gas.

The reactivity of metal surfaces comes from the adsorption of any inhibiting compounds present on them. Indeed, the importance of calculating the energy gap ( $\Delta E_{gap}$ ) for an inhibitor is a key indicator. Lower  $\Delta E_{gap}$  values indicate more reactive inhibitors. This makes us admit that the best corrosion inhibitors have low  $\Delta E_{gap}$  values [45]. Table 8 reveals that corrosion prevention by HAp in water is better.



Molecules with the lowest global hardness values are believed to be excellent metal corrosion inhibitors in corrosive medium. In contrast, The inhibitor adsorption onto a metal surface takes place in the 'molecule's part with the highest electronegativity and softness [46]. Therefore, according to the aforementioned descriptors, the variation order of the inhibitory efficiency of the studied HAp molecule is preferred in water.

The electrophilicity index is another descriptor that shows the molecule's tendency to receive electrons. On the other hand, nucleophilicity is the physical inverse of electrophilicity [17]. Indeed, molecules with high electrophilicity are ineffective against corrosion, and those with high nucleophilicity are effective corrosion inhibitors. Therefore, according to Table 8, the inhibiting efficiency of the HAp molecule in water is greater than that of this molecule in gas.

The  $\Delta N$  measures electron transfer between a metal and a molecule. When  $\Delta N < 0$ , electrons move from metal to molecule; when 'it's greater than zero, electrons move from molecule to steel. The greater value of  $\Delta N$  demonstrates the greater the ability to give electrons to the surface of the metal [47]. Given the  $\Delta N$  values (Table 8) calculated for the molecule studied, the best inhibition efficiency can be given for HAp in water.

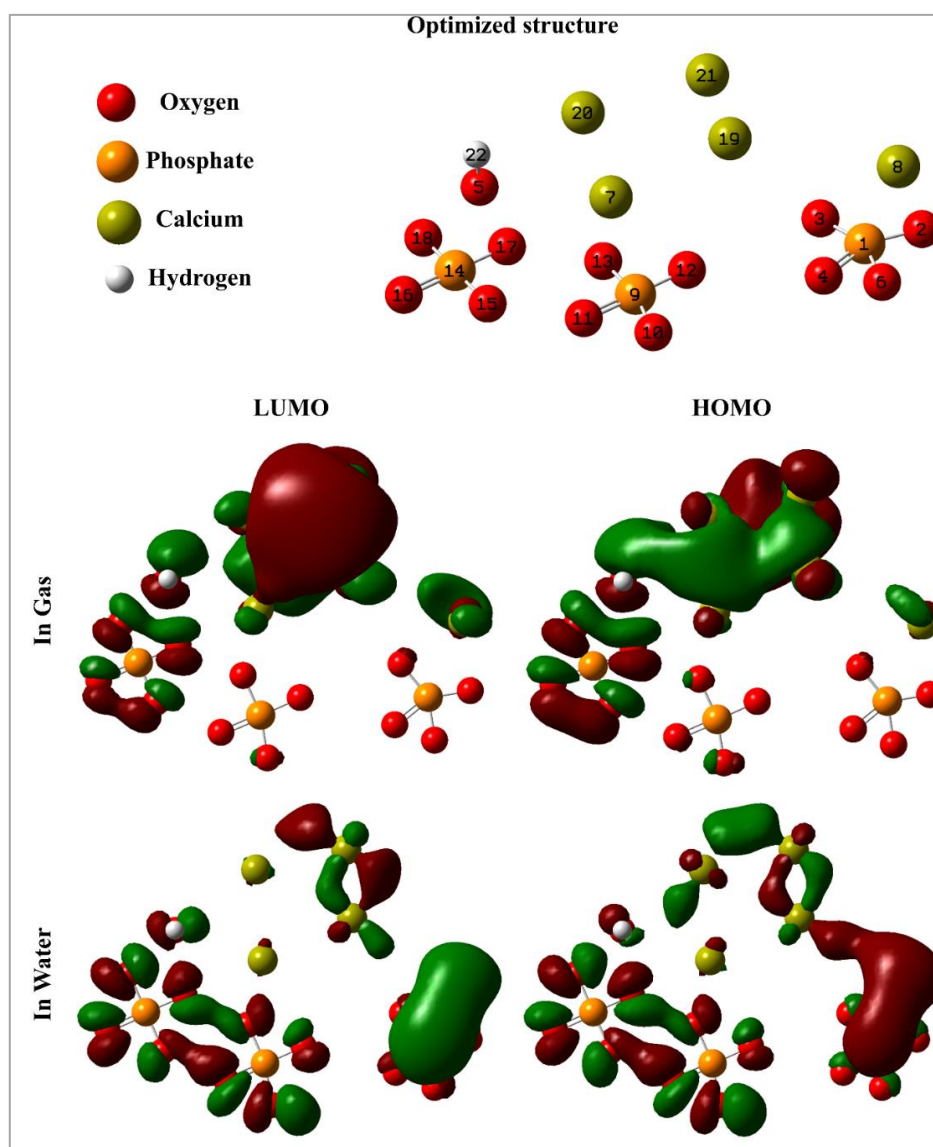


**Figure 14.** Repartition of HOMO/LUMO and optimized structure of hydroxyapatite obtained from DFT at the B3LYP with 6-311++G(d, p) basis.

**Table 8.** Chemical quantum parameters of studied hydroxyapatite compounds calculated at the B3LYP with 6-311++G(d, p) basis.

Inhibitor	$E_{HOMO}$ (eV)	$E_{LUMO}$ (eV)	$\Delta E_{gap}$ (eV)	$I_p$ (eV)	$E_A$ (eV)	$\chi$ (eV)	$\eta$ (eV)	$\omega$ (eV)	$\epsilon$ (eV)	$\sigma$ (eV) <sup>-1</sup>	$\Delta N$
HAp in gas	-4,435	-3,813	0,622	4,435	3,813	4,124	0,311	27,341	0,037	3,215	1,119
HAp in water	-1,721	-1,311	0,410	1,721	1,311	1,516	0,205	5,610	0,178	4,881	8,062

Looking at the Fukui indices, the high values of negative Fukui indices ( $f^-$ ) are responsible for electrophilic attacks (electron-donating character), while the high values of positive Fukui indices ( $f^+$ ) are responsible for nucleophilic attacks (electron-accepting character) [28]. As shown in Fig. 15 and Table 9, it can be seen that for HAp in gas, the high values of  $f^-$  and  $f^+$  are located on the Ca(8), Ca(20), and Ca(21). The HAp in water give high  $f^+$  indices in Ca(21). While the high  $f^-$  Indices are located on the Ca(7), Ca(19), Ca(20), and Ca(21), indicating that calcium in this compound has an excellent electron-donating character. These findings confirm the ability of this molecule inhibitor to react with the iron surface.

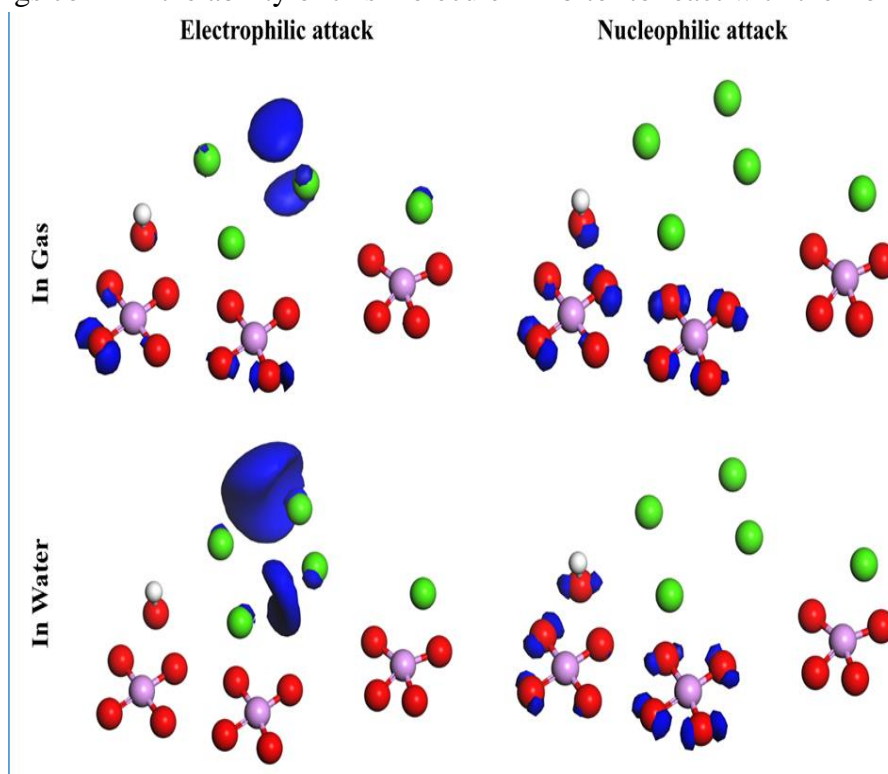


**Figure 15** Fukui indices (FI) of hydroxyapatite calculated by DFT (DMol<sup>3</sup>).

**Table 9.** Calculated Fukui indices of nucleophilic ( $f^+$ ) and electrophilic ( $f^-$ ) behaviors for hydroxyapatite.

Atom	In Gas		In Water	
	$f^-$	$f^+$	$f^-$	$f^+$
P (1)	0.012	0.012	0.007	0.003
O (2)	0.012	0.011	0.003	0.002
O (3)	-0.001	-0.001	0.005	0.000
O (4)	0.004	0.005	0.002	0.002
O (5)	0.022	0.021	0.005	0.041
O (6)	0.016	0.016	0.003	0.003
Ca (7)	0.035	0.034	0.137	0.040
Ca (8)	0.224	0.230	0.063	0.050
P (9)	0.024	0.024	0.009	0.058

Atom	In Gas		In Water	
	$f^-$	$f^+$	$f^-$	$f^+$
O (10)	0.041	0.041	0.009	0.099
O (11)	0.026	0.026	0.008	0.078
O (12)	0.024	0.023	0.004	0.065
O (13)	0.015	0.014	0.002	0.044
P (14)	0.025	0.024	0.006	0.044
O (15)	0.022	0.021	0.007	0.039
O (16)	0.054	0.054	0.008	0.070
O (17)	0.016	0.017	0.003	0.023
O (18)	0.024	0.023	0.006	0.070
Ca (19)	0.080	0.080	0.134	0.046
Ca (20)	0.153	0.154	0.182	0.086
Ca (21)	0.158	0.158	0.394	0.115
H (22)	0.013	0.012	0.003	0.022

### 3.6.2. Molecular dynamics simulations.

By analyzing the data and patterns obtained from the MD simulations, it is possible to understand more precisely how corrosion inhibitors bind to metals. Indeed, these calculations and results provide an in-depth insight into the interactions of inhibitor molecules with metals. Fig. 16 displays the side and top views of two corrosion inhibitor molecules (HAp in vacuum and in water) on the Fe (110) surface. Each 'inhibitor's energy of interaction and binding is shown in Table 10.

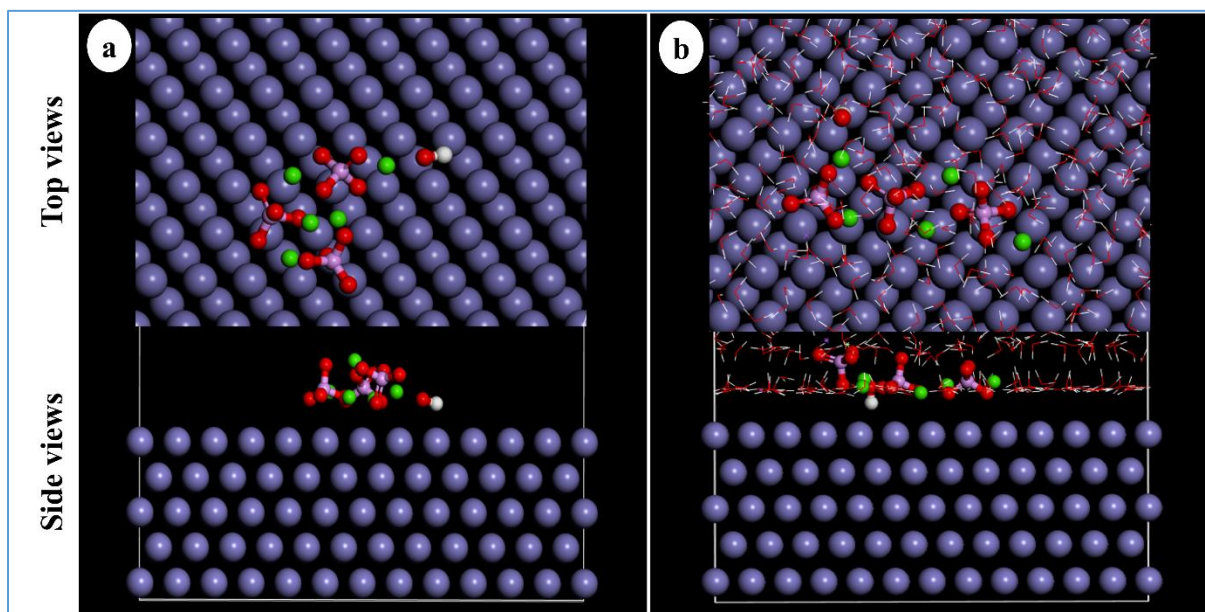


**Figure 16.** Configurations of hydroxyapatite compounds adsorption on the iron surface obtained by MD simulations. (a) In vacuum and (b) In the presence of water molecules.

The amount of energy needed to interact with iron determines the strength of an inhibitor. Studying the effectiveness of inhibitors shows that the more negative their  $E_{interaction}$  values are, the more spontaneously they adsorb on the iron surface. This indicates that inhibitors perform better when they have a better possibility to interact with the iron surface. The negative interaction energies of HAp presented in Table 10 show the capacity of this molecule to bind to the steel surface and create an anticorrosive layer over the iron surface. The order of decrease in interaction energy is HAp in water (-9007,01 kcal/mol) < HAp in vacuum

(-974,12 kcal/mol). Based on these values, it can be seen that HAp in water possesses the greatest binding energy and, therefore, has a strong inhibitory power for iron surfaces.

It can be noted that the MD simulations are in the same trend as that observed for the chemical quantum descriptors, which produce results consistent with corrosion inhibition performance. Overall, the results of these theoretical studies confirm the inhibition efficiency that has been reported experimentally.

**Table 10.** The different energetic outputs (kcal/mol) derived from MD simulations of inhibiting hydroxyapatite over the iron substrate.

Simulations models	E <sub>interaction</sub> (KJ/mol)	E <sub>binding</sub> (KJ/mol)
Fe (110) + Hydroxyapatite	-974,12	974,12
Fe (110) + Hydroxyapatite + 500 H <sub>2</sub> O + 5 Na <sup>+</sup> + 5 Cl <sup>-</sup>	-9007,01	9007,01

#### 4. Conclusions

The hydroxyapatite was synthesized by co-precipitation in an aqueous medium and then characterized by structural, microstructural, and chemical techniques. The product obtained reveals a Ca/P=1.67 ratio characteristic of stoichiometric HAp. Furthermore, the evaluation of HAp as a steel corrosion inhibitor in 3% NaCl indicated high protection of the steel. The open circuit potential analysis of the steel indicates a shift in corrosion potential in the existence of HAp relative to the blank medium, leading to the formation of a layer at the steel interface. Stationary polarization curves of the metal in 3% NaCl revealed that HAp is acting as a mixed type having a cathodic predominance with an optimum efficiency of 91% when the concentration is 100 ppm. The examination of the impedance diagrams of HAp in 3% NaCl shows that the corrosion mechanism is unchanged through the addition of HAp and that the spectra consist of two capacitive loops, one at high frequency (film adsorption) and the other at low frequency (charge transfer). These findings are similar to those found in the PDP analysis. The inhibitory efficacy of HAp in a 3% NaCl medium was slightly influenced by increasing temperature but was still significant in the temperature range studied. The HAp adsorption molecule at the metal surface is produced through the physical adsorption type and follows the Langmuir isotherm. The surface morphology of the steel using SEM/EDX analysis affirms the good anticorrosive power of HAp towards steel in a 3% NaCl environment through the construction of a barrier layer at the interface, which retards the corrosion rate of the steel. In addition, experimental and theoretical studies have shown that the corrosion-inhibiting HAp molecule has a high tendency to adsorb on the iron surface. Molecular dynamics simulations and quantum mechanical descriptors supported the theoretical study. Combining these results with experimental results reveals that HAp can be exploited as an environmentally friendly inhibitor for steel corrosion in 3% NaCl.

#### Funding

This research did not receive any specific grant from funding agencies in the public, commercial, or not-for-profit sectors.

#### Acknowledgments

This research has no acknowledgment.



## Conflicts of Interest

Dr. FERRA Nouhaila, corresponding author of the manuscript titled " Theoretical Investigation and Electrochemical Study of Stoichiometric Hydroxyapatite as an Eco-friendly Corrosion Inhibitor for Steel in 3% NaCl " submitting to *Biointerface Research in Applied Chemistry* do hereby declare, that there is no conflict of interest (either academic or financial) associated with the manuscript, either partly or as a whole.

## References

1. Chambard, M.; Marsan, O.; Charvillat, C.; Grossin, D.; Fort, P.; Rey, C.; Gitzhofer, F.; Bertrand, G. Effect of the deposition route on the microstructure of plasma-sprayed hydroxyapatite coatings. *Surf. Coat. Technol.* **2019**, *371*, 68–77, <https://doi.org/10.1016/j.surfcoat.2019.01.027>.
2. Asemabadi, Z.; Korrani, A.M.; Dolatabadi, M.M.; Mohammadloo, H.E.; Sarabi, A.A.; Roshan, Sh. Modification of hydroxyapatite coating in the presence of adipic acid for Mg-based implant application. *Prog. Org. Coat.* **2022**, *172*, 107088, <https://doi.org/10.1016/j.porgcoat.2022.107088>.
3. Hussin, M.S.F.; Abdullah, H.Z.; Idris, M.I.; Wahap, M.A.A. Extraction of natural hydroxyapatite for biomedical applications—A review. *Heliyon* **2022**, *8*, e10356, <https://doi.org/10.1016/j.heliyon.2022.e10356>.
4. Xiao, H.; Arsecularatne, J.A.; Zheng, J.; Hoffman, M.J.; Zhou, Z. Effect of HAP crystallite orientation upon corrosion and tribocorrosion behavior of bovine and human dental enamel. *Corros. Sci.* **2021**, *190*, 109670, <https://doi.org/10.1016/j.corsci.2021.109670>.
5. Cacciotti, I. Multisubstituted hydroxyapatite powders and coatings: The influence of the codoping on the hydroxyapatite performances. *Int. J. Appl. Ceram. Technol.* **2019**, *16*, 1864–1884, <https://doi.org/10.1111/ijac.13229>.
6. Ouakki, M.; Galai, M.; Cherkaoui, M.; Rifi, E.H.; Hatim, Z. Inorganic compound (Apatite doped by Mg and Na) as a corrosion inhibitor for mild steel in phosphoric acidic medium. *Anal. Bioanal. Electrochem.* **2018**, *10*, 943-960.
7. Ferraa, N.; Ouakki, M.; Cherkaoui, M.; Ziatni, M.B. Synthesis, Characterization and Evaluation of Apatitic Tricalcium Phosphate as a Corrosion Inhibitor for Carbon Steel in 3 wt% NaCl. *J. Bio. Tribo. Corros.* **2022**, *8*, 23, <https://doi.org/10.1007/s40735-021-00622-4>.
8. Mzioud, K.; Habsaoui, A.; Ouakki, M.; Galai, M.; El Fartah, S.; Touhami, M.E. Inhibition of copper corrosion by the essential oil of *Allium sativum* in 0.5M H<sub>2</sub>SO<sub>4</sub> solutions. *SN Appl. Sci.* **2020**, *2*, 1611, <https://doi.org/10.1007/s42452-020-03393-8>.
9. Zehra, B.F.; Said, A.; Eddine, H.M.; Hamid, E.; Najat, H.; Rachid, N.; Toumert, L.I. *Crataegus oxyacantha* leaves extract for carbon steel protection against corrosion in 1M HCl: Characterization, electrochemical, theoretical research, and surface analysis. *J. Mol. Struct.* **2022**, *1259*, 132737, <https://doi.org/10.1016/j.molstruc.2022.132737>.
10. Obot, I.B.; Ul-Haq, M.I.; Sorour, A.A.; Alanazi, N.M.; Al-Abeedi, T.M.; Ali, S.A.; Al-Muallem, H.A. Modified-polyaspartic acid derivatives as effective corrosion inhibitor for C1018 steel in 3.5% NaCl saturated CO<sub>2</sub> brine solution. *J. Taiwan Inst. Chem. Eng.* **2022**, *135*, 104393, <https://doi.org/10.1016/j.jtice.2022.104393>.
11. Shao, H.; Yin, X.; Zhang, K.; Yang, W.; Chen, Y.; Liu, Y. N-[2-(3-indolyl)ethyl]-cinnamamide synthesized from cinnamomum cassia presl and alkaloid tryptamine as green corrosion inhibitor for Q235 steel in acidic medium. *J. Mater. Res. Technol.* **2022**, *20*, 916–933, <https://doi.org/10.1016/j.jmrt.2022.07.122>.
12. Aslam, R.; Mobin, M.; Zehra, S.; Aslam, J. A comprehensive review of corrosion inhibitors employed to mitigate stainless steel corrosion in different environments. *J. Mol. Liq.* **2022**, *364*, 119992, <https://doi.org/10.1016/j.molliq.2022.119992>.
13. Rey, C.; Lian, J.I.; Grympas, M.; Shapiro, F.; Zulkerg, L.; Glimcher, M.J. *Tissue Res* **1989**, *21*, 267.
14. Abdelhadi, E.R.; Mourabet, M.; Boujaady, H.E.; Bennani-Ziatni, M.; Hamri, R.E.; Abderrahim, T. Adsorption des acides aminés essentiels et leur mélange sur l'hydroxyapatite mal cristallisée (Adsorption of some essential amino acids and their mixture onto poorly crystalline hydroxyapatite). *J. Mater. Environ. Sci* **2014**, *5*, 1442-1453.
15. Becke, A.D. Density -functional exchange- energy approximation with correct asymptotic behavior, *PHYSICAL REVIEW A.* **1988**, *38*, 3098–3100. <https://doi.org/10.1103/PhysRevA.38.3098>

16. Skyner, R.E.; McDonagh, J.L.; Groom, C.R.; van Mourik, T.; Mitchell, J.B.O. A review of methods for the calculation of solution free energies and the modelling of systems in solution. *Phys. Chem. Chem. Phys.* **2015**, *17*, 6174–6191, <https://doi.org/10.1039/C5CP00288E>.
17. Madkour, L.H.; Kaya, S.; Guo, L.; Kaya, C. Quantum chemical calculations, molecular dynamic (MD) simulations and experimental studies of using some azo dyes as corrosion inhibitors for iron. Part 2: Bis-azo dye derivatives. *J. Mol. Struct.* **2018**, *1163*, 397–417. <https://doi.org/10.1016/j.molstruc.2018.03.013>.
18. Dehghani, A.; Bahlakeh, G.; Ramezanzadeh, B.; Ramezanzadeh, M. Integrated modeling and electrochemical study of *Myrobalan* extract for mild steel corrosion retardation in acidizing media. *J. Mol. Liq.* **2020**, *298*, 112046, <https://doi.org/10.1016/j.molliq.2019.112046>.
19. Chugh, B.; Singh, A.K.; Chaouiki, A.; Salghi, R.; Thakur, S.; Pani, B. A comprehensive study about anti-corrosion behaviour of pyrazine carbohydrazide: Gravimetric, electrochemical, surface and theoretical study. *J. Mol. Liq.* **2020**, *299*, 112160, <https://doi.org/10.1016/j.molliq.2019.112160>.
20. Olasunkanmi, L.O.; Obot, I.B.; Kabanda, M.M.; Ebenso, E.E. Some Quinoxalin-6-yl Derivatives as Corrosion Inhibitors for Mild Steel in Hydrochloric Acid: Experimental and Theoretical Studies. *J. Phys. Chem. C* **2015**, *119*, 16004–16019, <https://doi.org/10.1021/acs.jpcc.5b03285>.
21. Benzidia, B.; Barbouchi, M.; Hsissou, R.; Zouarhi, M.; Erramli, H.; Hajjaji, N. A combined experimental and theoretical study of green corrosion inhibition of bronze B66 in 3% NaCl solution by *Aloe saponaria* (syn. *Aloe maculata*) tannin extract. *Curr. Res. Green Sustain. Chem.* **2022**, *5*, 100299, <https://doi.org/10.1016/j.crgsc.2022.100299>.
22. Sun, H.; Ren, P.; Fried, J. R. The COMPASS force field: parameterization and validation for phosphazenes. *Computational and Theoretical Polymer Science*, **1998**, *8*, 229-246. [https://doi.org/10.1016/S1089-3156\(98\)00042-7](https://doi.org/10.1016/S1089-3156(98)00042-7)
23. Hsissou, R.; Azogagh, M.; Benhiba, F.; Echihi, S.; Galai, M.; Shaim, A.; Bahaj, H.; Briche, S.; Kaya, S.; Serdaroğlu, G.; Zarrouk, A.; Touhami, M.E.; Rafik, M. Insight of development of two cured epoxy polymer composite coatings as highly protective efficiency for carbon steel in sodium chloride solution: DFT, RDF, FFV and MD approaches. *J. Mol. Liq.* **2022**, *360*, 119406, <https://doi.org/10.1016/j.molliq.2022.119406>.
24. El Rhilassi, A.; Mourabet, M.; Bennani-Ziatni, M.; El Hamri, R.; Taitai, A. Interaction of some essential amino acids with synthesized poorly crystalline hydroxyapatite. *J. Saudi Chem. Soc.* **2016**, *20*, S632–S640, <https://doi.org/10.1016/j.jscs.2013.05.003>.
25. Benchikh, A.; Belkacemi, S.; Maizia, R.; Mezian, K.; Makhloufi, L.; Saidani, B. Chemical synthesis and characterization of a soluble copolymer poly (methoxyaniline-co-orthotoluidine), application as corrosion inhibitor of carbon steel in 3% NaCl medium. *J. Mol. Struct.* **2023**, *1274*, 134562, <https://doi.org/10.1016/j.molstruc.2022.134562>.
26. Saraswat, V.; Yadav, M. Computational and electrochemical analysis on quinoxalines as corrosion inhibitors for mild steel in acidic medium. *J. Mol. Liq.* **2020**, *297*, 111883, <https://doi.org/10.1016/j.molliq.2019.111883>.
27. Dagdag, O.; El Gouri, M.; Galai, M.; Touhami, M.E.; Essamri, A.; Elharfi, A. Influence of a derivative of cyclotriphosphazene as a corrosion inhibitor for carbon steel in 3% NaCl medium. *J. Chem. Pharm. Res.* **2015**, *7*, 712-720.
28. Barbouchi, M.; Benzidia, B.; Aouidate, A.; Ghaleb, A.; El Idrissi, M.; Choukrad, M. Theoretical modeling and experimental studies of Terebinth extracts as green corrosion inhibitor for iron in 3% NaCl medium. *J. King Saud Univ. Sci.* **2020**, *32*, 2995–3004, <https://doi.org/10.1016/j.jksus.2020.08.004>.
29. Guo, X.; Huang, H.; Liu, D. The inhibition mechanism and adsorption behavior of three purine derivatives on the corrosion of copper in alkaline artificial seawater: Structure and performance. *Colloids Surf. A: Physicochem. Eng. Asp.* **2021**, *622*, 126644, <https://doi.org/10.1016/j.colsurfa.2021.126644>.
30. El-Aouni, N.; Hsissou, R.; Safi, Z.; About, S.; Benhiba, F.; El Azzaoui, J.; Haldhar, R.; Wazzan, N.; Guo, L.; Erramli, H.; Elharfi, A.; El Bachiri, A.; Rafik, M. Performance of two new epoxy resins as potential corrosion inhibitors for carbon steel in 1M HCl medium: Combining experimental and computational approaches. *Colloids Surf. A: Physicochem. Eng. Asp.* **2021**, *626*, 127066, <https://doi.org/10.1016/j.colsurfa.2021.127066>.
31. Fekri, M.H.; Omidali, F.; Alemnezhad, M.M.; Ghaffarinejad, A. Turnip peel extract as green corrosion bio-inhibitor for copper in 3.5% NaCl solution. *Mater. Chem. Phys.* **2022**, *286*, 126150, <https://doi.org/10.1016/j.matchemphys.2022.126150>.
32. Elqars, E.; Oubella, A.; Byadi, S.; Hachim, M.E.; Auhmani, A.; Guennoun, M.; Essadki, A.; Riahi, A.; Robert, A.; Itto, M.Y.A.; Nbigui, T. Synthesis, spectroscopic characterization, and prevention of carbon steel



- corrosion in hydrochloric acid of a new bis-isoxazoline-carvone. *J. Mol. Struct.* **2022**, *1256*, 132526, <https://doi.org/10.1016/j.molstruc.2022.132526>.
33. Tristijanto, H.; Ilman, M.N.; Iswanto, P.T. Corrosion Inhibition of Welded of X – 52 Steel Pipelines by Sodium Molybdate in 3.5% NaCl Solution. *Egypt. J. Pet.* **2020**, *29*, 155–162, <https://doi.org/10.1016/j.ejpe.2020.02.001>.
34. Tan, B.; Zhang, S.; Qiang, Y.; Guo, L.; Feng, L.; Liao, C.; Xu, Y.; Chen, S. A combined experimental and theoretical study of the inhibition effect of three disulfide-based flavouring agents for copper corrosion in 0.5 M sulfuric acid. *J. Colloid Interface Sci.* **2018**, *526*, 268–280, <https://doi.org/10.1016/j.jcis.2018.04.092>.
35. Anusuya, N.; Saranya, J.; Sounthari, P.; Zarrouk, A.; Chitra, S. Corrosion inhibition and adsorption behaviour of some bis-pyrimidine derivatives on mild steel in acidic medium., *J. Mol. Liq.* **2017**, *225*, 406–417, <https://doi.org/10.1016/j.molliq.2016.11.015>.
36. Asfia, M.P.; Rezaei, M.; Bahlakeh, G. Corrosion prevention of AISI 304 stainless steel in hydrochloric acid medium using garlic extract as a green corrosion inhibitor: Electrochemical and theoretical studies. *J. Mol. Liq.* **2020**, *315*, 113679, <https://doi.org/10.1016/j.molliq.2020.113679>.
37. Aaad, H.E.; Galai, M.; Ouakki, M.; Elgendy, A.; Touhami, M.E.; Chahine, A. Improvement of the corrosion resistance of mild steel in sulfuric acid by new organic-inorganic hybrids of Benzimidazole-Pyrophosphate: Facile synthesis, characterization, experimental and theoretical calculations (DFT and MC). *Surf. Interfaces* **2021**, *24*, 101084, <https://doi.org/10.1016/j.surfin.2021.101084>.
38. Mzioud, K.; Habsaoui, A.; Rached, S.; Lachhab, R.; Dkhireche, N.; Ouakki, M.; Galai, M.; El Fartah, S.; Touhami, M.E. Synergistic Effect from Allium Sativum Essential Oil and Diethylthiourea for Corrosion Inhibition of Carbon Steel in 0.5 M H<sub>2</sub>SO<sub>4</sub> Medium in Book Proceedings of the Sixth International Symposium on Dielectric Materials and Applications (ISyDMA'6), Vaseashta, A., Achour, M.E., Mabrouki, M., Fasquelle, D., Tachafine, A., Eds.; Springer International Publishing, Cham, **2022**; pp. 251–266, [https://doi.org/10.1007/978-3-031-11397-0\\_23](https://doi.org/10.1007/978-3-031-11397-0_23).
39. Ferraa, N.; Ouakki, M.; Cherkaoui, M.; Ziatni, M.B. Study of the Inhibitory Action of Apatitic Tricalcium Phosphate on Carbon Steel in Two Acidic Media (HCl 1.0 M and H<sub>2</sub>SO<sub>4</sub> 0.5 M) in Book Proceedings of the Sixth International Symposium on Dielectric Materials and Applications (ISyDMA'6), Vaseashta, A., Achour, M.E., Mabrouki, M., Fasquelle, D., Tachafine, A., Eds.; Springer International Publishing, Cham, **2022**; pp. 159–176, [https://doi.org/10.1007/978-3-031-11397-0\\_14](https://doi.org/10.1007/978-3-031-11397-0_14).
40. Zhao, T.; Munis, A.; Zheng, M.; Hu, J.; Teng, H.; Wei, L. 2-(2-Pentadecyl-4, 5-dihydro-1H-imidazol-1-yl)ethanol as a sustainable inhibitor for copper corrosion in molten hydrated phase change materials. *J. Mol. Liq.* **2020**, *316*, 113927, <https://doi.org/10.1016/j.molliq.2020.113927>.
41. Zheng, H.; Zhang, B.; Wang, X.; Lu, Y.; Li, F.; Li, C. Improved corrosion resistance of carbon steel in soft water with dendritic-polymer corrosion inhibitors. *Chem. Eng. J.* **2023**, *452*, 139043, <https://doi.org/10.1016/j.cej.2022.139043>.
42. Li, X.; Deng, S.; Fu, H. Triazolyl blue tetrazolium bromide as a novel corrosion inhibitor for steel in HCl and H<sub>2</sub>SO<sub>4</sub> solutions. *Corros. Sci.* **2011**, *53*, 302–309, <https://doi.org/10.1016/j.corsci.2010.09.036>.
43. de Souza, F.S.; Giacomelli, C.; Gonçalves, R.S.; Spinelli, A. Adsorption behavior of caffeine as a green corrosion inhibitor for copper. *Mater. Sci. Eng. C* **2012**, *32*, 2436–2444, <https://doi.org/10.1016/j.msec.2012.07.019>.
44. Wang, Q.; Liu, L.; Zhang, Q.; Wu, X.; Zheng, H.; Gao, P.; Zeng, G.; Yan, Z.; Sun, Y.; Li, Z.; Li, X. Insight into the anti-corrosion performance of *Artemisia argyi* leaves extract as eco-friendly corrosion inhibitor for carbon steel in HCl medium. *Sustain. Chem. Pharm.* **2022**, *27*, 100710, <https://doi.org/10.1016/j.scp.2022.100710>.
45. Ouakki, M.; Galai, M.; Rbaa, M.; Abousalem, A.S.; Lakhri, B.; Rifi, E.H.; Cherkaoui, M. Quantum chemical and experimental evaluation of the inhibitory action of two imidazole derivatives on mild steel corrosion in sulphuric acid medium. *Heliyon* **2019**, *5*, e02759, <https://doi.org/10.1016/j.heliyon.2019.e02759>.
46. Singh, R.; Prasad, D.; Safi, Z.; Wazzan, N.; Guo, L. De-scaling, experimental, DFT, and MD-simulation studies of unwanted growing plant as natural corrosion inhibitor for SS-410 in acid medium. *Colloids Surf. A: Physicochem. Eng. Asp.* **2022**, *649*, 129333, <https://doi.org/10.1016/j.colsurfa.2022.129333>.
47. Haldhar, R.; Prasad, D.; Saxena, A. *Myristica fragrans* extract as an eco-friendly corrosion inhibitor for mild steel in 0.5 M H<sub>2</sub>SO<sub>4</sub> solution. *J. Environ. Chem. Eng.* **2018**, *6*, 2290–2301, <https://doi.org/10.1016/j.jece.2018.03.023>.